THE AMERICAN SOCIETY OF MECHANICAL ENGINEERS
345 E. 47th St., New York, N.Y. 10017

98-GT-464

COMPLEMENTARY VELOCITY AND HEAT TRANSFER MEASUREMENTS IN A ROTATING COOLING PASSAGE WITH SMOOTH WALLS

Jeffrey P. Bons
Department of Aeronautics and Astronautics
Air Force Institute of Technology
Wright-Patterson AFB, OH 45433

Jack L. Kerrebrock
Department of Aeronautics and Astronautics
Massachusetts Institute of Technology
Cambridge, MA 02139

ABSTRACT

An experimental investigation was conducted on the internal flowfield of a simulated smooth-wall turbine blade cooling passage. The square cross-sectioned passage was manufactured from quartz for optical accessibility. Velocity measurements were taken using Particle Image Velocimetry for both heated and non-heated cases. Thin film resistive heaters on all four exterior walls of the passage allowed heat to be added to the coolant flow without obstructing laser access. Under the same conditions, an infrared detector with associated optics collected wall temperature data for use in calculating local Nusselt number. The test section was operated with radial outward flow and at values of Reynolds number and Rotation number typical of a small turbine blade. The density ratio was 0.27. Velocity data for the non-heated case document the evolution of the coriolis-induced double vortex. The vortex has the effect of disproportionately increasing the leading side boundary layer thickness. Also, the streamwise component of the coriolis acceleration creates a considerably thinned side wall boundary layer. Additionally, these data reveal a highly unsteady, turbulent flowfield in the cooling passage. Velocity data for the heated case show a strongly distorted streamwise profile indicative of a buoyancy effect on the leading side. The coriolis vortex is the mechanism for the accumulation of stagnant flow on the leading side of the passage. Heat transfer data show a maximum factor of two difference in the Nusselt number from trailing side to leading side. A first-order estimate of this heat transfer disparity based on the measured boundary layer edge velocity yields approximately the same factor of two. A momentum integral model was developed for data interpretation which accounts for coriolis and buoyancy effects. Calculated streamwise profiles and secondary flows match the experimental data well. The model, the velocity data, and the heat transfer data combine to strongly suggest the presence of separated flow on the leading wall starting at about five hydraulic diameters from the channel inlet for the conditions studied.

NOMENCLATURE

Bo - Buoyancy param. = $\beta(T-T_\infty)R_m\Omega^2d/u^2$
d - hydraulic diameter = 4 x area/perimeter
d.r. - density ratio = $(T_w-T_{in})/T_w$
k - gas thermal conductivity
l - passage length
n - power law profile exponent
Nu - Nusselt number = $qd/k_{film}(T_w-T_{film})$
Pr - Prandtl number = ν/α
q - surface heat flux
r or R - radial distance to axis of rotation
R_m - mean radius of test section
Re - passage Reynolds number = du_{in}/ν
Rot - Rotation number = $\Omega d/u$
Ra_Ω - rotational Rayleigh number
T - local static temperature
u - x component of velocity
v - y component of velocity
v_o - velocity of wall injected boundary fluid
V - complete velocity vector
w - z component of velocity
x - radial (streamwise) direction in passage
y - axis parallel with axis of rotation
z - crossflow direction in passage
α - thermal diffusivity

Presented at the International Gas Turbine & Aeroengine Congress & Exhibition
Stockholm, Sweden — June 2–June 5, 1998
This paper has been accepted for publication in the Transactions of the ASME
Discussion of it will be accepted at ASME Headquarters until September 30, 1998

β - volumetric expansion coefficient
δ - boundary layer thickness
λ - wavelength of radiation
μ - viscosity
ν - kinematic viscosity
θ - boundary layer momentum thickness
ρ - fluid density
τ_o - wall shear stress
Ω - rotational frequency

subscripts
BS - back side passage wall
cor - Coriolis
film - average of wall and bulk
FS - front side passage wall
in - passage inlet conditions
inf - freestream conditions
LS - leading passage wall
TS - trailing passage wall
∞ - freestream conditions

INTRODUCTION

The hot section of a modern gas turbine engine is a challenging design environment. The turbine is required to operate with high inlet temperatures and aggressive blade loading to provide high specific power. These demands conflict directly with the limitations of engineering materials. To resolve this conflict, since the 1960s bleed air from the compressor has been used to cool turbine vanes, blades, casings, and disks. With cooling, engine designers have realized a 300-500°C increase in operating turbine inlet temperatures beyond previous limits.

To cool the rotating turbine blade in particular, cooling air flows through a network of serpentine cooling passages oriented along the span of the blade. Raised steps (or ribs) are commonly used to trip the boundary layers and augment the heat transfer from the metal walls in these internal cooling passages. Modern turbine design depends on reliable cooling schemes to achieve performance levels beyond the capabilities of blading materials alone. Even a deficiency of coolant creates aggravated thermal stresses in the highly stressed rotating blade which can result in severe oxidation, creep, and local fatigue of the blade. Because of its critical role, considerable effort has been expended to accurately predict the performance of turbine internal cooling. Design engineers realized early on, however, that because of the rotating turbine frame of reference, standard pipe flow correlations for heat transfer were inadequate. Rotation introduces Coriolis and buoyancy accelerations which create secondary flow vortices and skew the mean flow profile. These flow non-uniformities result in non-homogeneous heat transfer from the different passage walls depending on their orientation (as depicted in Figure 1).

Flow in a heated rotating passage can be characterized by the Reynolds number, Re, the Rotation number, Rot, and the Buoyancy

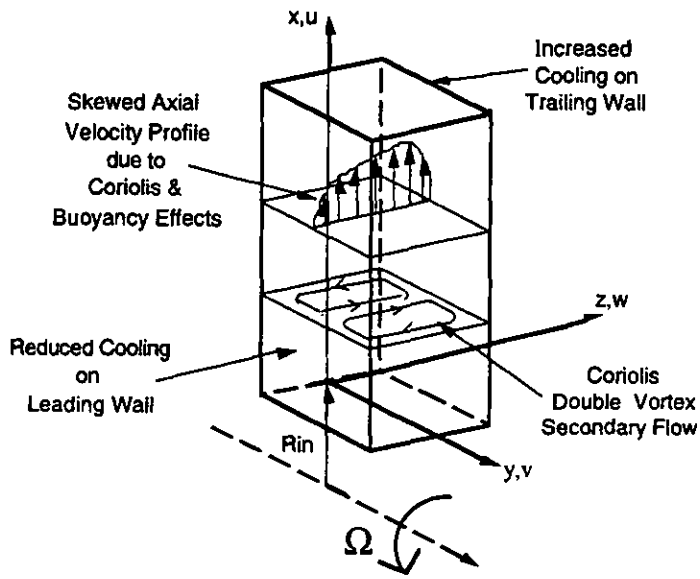

Figure 1: Schematic of Heated, Rotating Flow

parameter, Bo, defined as:

$$Re = \frac{\rho d u_{in}}{\mu} \qquad Rot = \frac{\Omega d}{u_{in}} \qquad Bo = \frac{T - T_{in}}{T}\left(\frac{\Omega d}{u_{in}}\right)^2 \frac{R_m}{d}$$

The Rotation number represents the ratio of Coriolis to inertial forces. The same ratio is sometimes expressed by its reciprocal, the Rossby number. The Buoyancy parameter represents the ratio of centrifugal to inertial forces and can also be expressed as

$$Bo = \frac{\beta(T - T_{in})\Omega^2 R_m d^3}{\nu\alpha}\left(\frac{\alpha}{\nu}\right)\left(\frac{\nu}{ud}\right)^2 = \frac{Ra_\Omega}{Pr\,Re^2}$$

where Ra_Ω is a rotational Rayleigh number (Morris, 1981). Ra_Ω is similar to the Rayleigh number from free convection analysis, the gravitational body force being replaced by a centrifugal body force. Alternatively, the Buoyancy parameter can be expressed in terms of the density ratio, defined as d.r. = $(T_w - T_{in})/T_w$, and the Rotation number squared. Since the bulk of turbine cooling research reported in the literature uses this density ratio to express the effect of centrifugal buoyancy (Wagner, 1991a, Han, 1992, Dutta, 1994, Tekriwal, 1996, and Hsieh, 1997), it is used here rather than the Buoyancy parameter.

The effects of these various parameters on the cooling passage Nusselt number have been the subject of numerous experimental and computational studies. As far back as the early 1950's, papers were being published on rotating duct flows. In a rotating passage (without heat) Moore (1967) showed that the primary effect of rotation was the creation of a double vortex secondary flow that shifts the core flow to the pressure surface for radial outflow. This creates higher skin friction and a thinner boundary layer on the pressure surface (trailing wall) and the opposite conditions on the suction surface (leading wall). With heat addition, centrifugal

buoyancy is introduced into the flow which precludes the summary use of Reynolds analogy to directly transport the effect of rotation on skin friction to heat transfer. Morris and Ayhan (1979) were first to incorporate the effect of centrifugal buoyancy in their interpretation of observed heat transfer phenomena in a rotating circular cross-section cooling tube. They proposed an empirical correlation for the passage mean Nu based on Bo.

In the last decade, interest in rotating heated passage flows has intensified with the direct application being turbine blade cooling passages. In 1989, Guidez (1989) published the results of experiments at Reynolds numbers higher than those previously reported, ensuring a turbulent pipe flow. He found the ratio of trailing side Nu to leading side Nu to be about two for Bo=0.08, and noted that this ratio decreased with increasing Re. Following Guidez, Wagner et al. (1991a&b, 1992) methodically studied the effects of Re, Rot, d.r., flow direction, and ribs on the cooling passage heat transfer. They used the density ratio to characterize the effects of centrifugal buoyancy and found that increasing d.r. augmented Nu on both trailing and leading sides. They measured a higher ratio of trailing to leading side Nu than Guidez for similar conditions. Their Nu data is normalized by a stationary Nu correlation ($Re^{0.8}$) for pipe flow, which they found to adequately remove Re dependency in the rotating data.

At the same time, Han et al. (1994) performed experiments using a facility which can be operated in either constant wall temperature or constant wall heat flux mode, (versus the Wagner and Johnson facility which is exclusively constant wall temperature and the Guidez facility which is constant wall heat flux). Han et al. found even larger effects of rotation and buoyancy: the trailing to leading side Nu ratio being nearly twice the value measured by Guidez for the same Bo condition. Han et al. also observed that the thermal boundary condition influences the measured heat transfer, i.e. the constant heat flux mode having a higher Nu on both leading and trailing side than the constant wall temperature case for the same density ratio. They reasoned that because a constant heat flux produces uneven wall temperatures, the buoyancy forces are unbalanced and create better cooling everywhere as these forces destabilize the passage flow.

These and other experimental findings have succeeded in mapping out many of the parametric trends in the performance of turbine cooling passages, but because of the wide spread in the results from different facilities (Figure 2) the cooling designer is still left without a clear understanding of the quantitative effect of rotation. This is because the underlying mechanisms causing these rotational effects on cooling are as yet unexplored. The wall heat transfer distribution is ultimately a product of the flowfield, and until recently none of the experimental work has measured the detailed velocity field inside the rotating heated passage. There are a number of researchers who have over the years made measurements in a rotating flowfield: Wagner and Velkoff (1972) with hot wires and more recently, Uellner and Roesner (1991), Berg et al. (1991), and Tse et al. (1995,1997) with laser diagnostics. But all of these are for non-heated rotating passages and therefore omit the buoyancy effect entirely. A 1997 publication by Hsieh et al. does present velocity data using LDV in a rotating passage with heating. However, the measurements are presented only along the passage centerline and show a marginal effect of rotation up to the maximum Rot of 0.06. In fact, the limited velocity data indicate a far greater effect of the passage ribs than the rotation effect at such low Rot. Moreover, with a passage inlet radius of only one test section diameter and a non-radial passage orientation, Hsieh's experimental configuration bears little resemblance to a turbine cooling passage. So, there is as yet no comprehensive picture of the flow inside a turbine blade cooling passage, information which is critical to understanding the passage heat transfer.

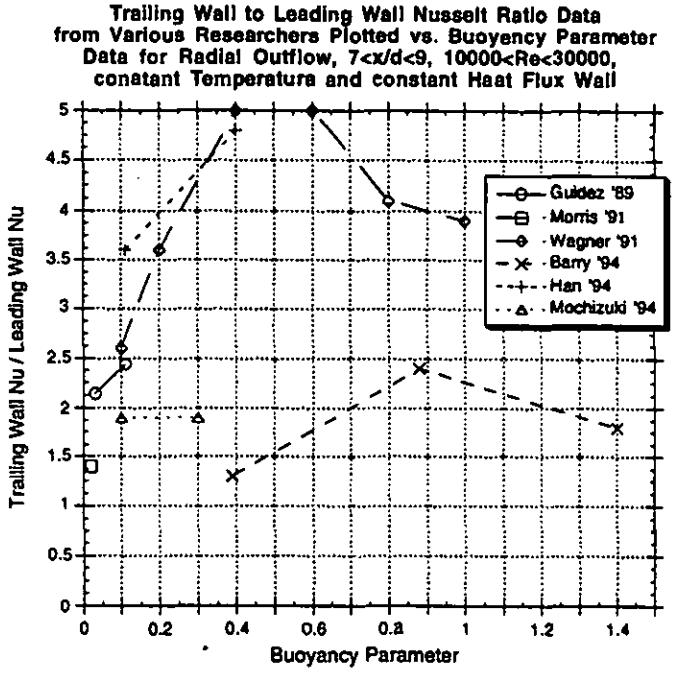

Figure 2: Rotating Heat Transfer Data from Various Researchers

On the computational front, researchers have predicted much of the experimentally measured effects of Coriolis and buoyancy. Based on Boyer (1965) and others' experimental findings that the rotating passage flow could be adequately characterized by an inviscid core region surrounded by thin wall layers, early analytical approaches employed either a perturbation method (Moore, 1967) or a momentum integral analysis (Mori and Nakayama, 1968 and Ito and Nanbu, 1971). More recently, 3-D Navier Stokes solvers have provided valuable flow insights including the discovery of an additional vortex pair (making 4 vortices in all) at high Rot (Iacovides and Launder, 1991) and the prediction of flow reversal at high Rot on the leading wall (Prakash and Zerkle, 1992). All of the heated rotating computations use the flow prediction to estimate Nu, which is then compared with experiment to assess code validity. A lack of detailed flow measurements in the heated, rotating frame has prevented direct comparison with velocity data and thus an adequate validation of the calculated flowfields.

The objective of this research is to provide the technical community with the first comprehensive measurements of velocity and heat transfer in a simulated turbine blade cooling passage. The method used to obtain the velocity measurements is particle image velocimetry (PIV). Thin film heaters on all four walls of a

transparent test section provide the necessary constant heat flux wall condition, while infrared imaging of the surface provides high spatial resolution measurement of heat transfer coefficient. This allows a direct correlation of flow phenomena to heat transfer phenomena without the ambiguities of different experimental facilities. These are the specific contributions of this paper.

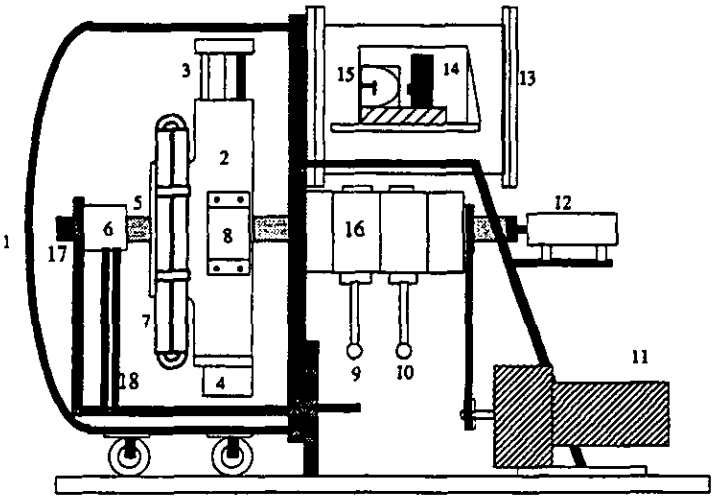

1. Vacuum Chamber / Protective Casing
2. Rotating Arm
3. Test Section and Mirrors
4. Balance Weight
5. Shaft
6. Power Slip Ring
7. Heat Exchangers
8. Onboard Instrumentation Box
9. Inlet flow
10. Outlet flow
11. Motor
12. Instrumentation Slip Ring
13. Housing
14. IR detector
15. Imaging system
16. Seals
17. Optical Encoder
18. Power wires

Figure 3: Schematic of Internal Cooling Test Facility

EXPERIMENTAL METHOD

The experimental facility used for this study is shown in Figure 3. The test section is mounted at the end of a 0.4m radius arm (R, /d=40) which spins in an evacuated chamber. Cooling air enters and exits the rotating arm and test section through seals located on the shaft. The test section (l/d=11.5) is manufactured from square-bore quartz tubing and mounts to the rotating arm as shown in Figure 4. Also indicated on Figure 4 are the tapered test section inlet, the flow conditioning screen, and the flow thermocouple ports at inlet and exit. The test section ID is 10mm square and the walls are ground and polished to a 1.5mm thickness. The center 90mm along each of the four sides is coated with a 10mm wide swath of Indium Tin Oxide (ITO). The coating thickness is nominally 4500Angstroms and it is applied with electron beam sputtering to the outside of the test section. Heat fluxes up to 5 W/cm^2 and wall temperatures up to 200C were achieved without film degradation. 8mm long Cr/Ni/Au busbars at either end of the ITO film provide uniform electrical contact to the ITO. The four sides are connected in a parallel circuit to allow resistive heating of the passage.

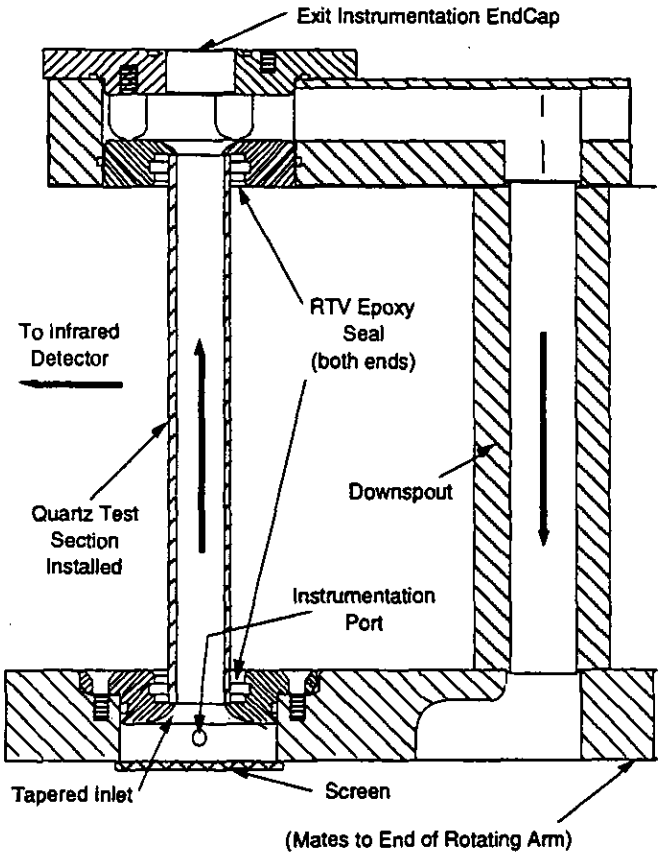

Figure 4: Schematic of Quartz Test Section Mounted in Housing on Rotating Arm

Due to a manufacturing complexity, the front side wall ITO sheet thickness is approximately 20% greater than the ITO thickness on the leading and trailing walls (which are roughly equivalent). This creates a lower resistance here, and a higher heat flux since more current passes through this part of the parallel resistance circuit. The back side wall's ITO thickness is conversely 20% less than the leading and trailing walls, causing a corresponding decrease in the heat flux here. The result is a higher heat load on the front internal wall by nearly 30% after accounting for temperature smearing through the test section walls. The effect of this heating imbalance is discussed in the results section.

The ITO film and quartz substrate provide 80% transmission at the visible wavelength of the laser used. Since the quartz is opaque in the IR spectrum, the capability of the IR scanning temperature measurement system was not compromised with the use of a transparent test section. The infrared detector is mounted on a two-axis traverse system with focusing optics (Figure 3). The spatial resolution of the detector and optics is 1mm^2. Two flat mirrors located at 90° to each other behind the test section provide optical access to all four sides of the rotating passage (Figure 5). The

horizontal traverse is used to move the focal point from one side to another and the vertical traverse allows measurement along the axis (x direction) of the passage.

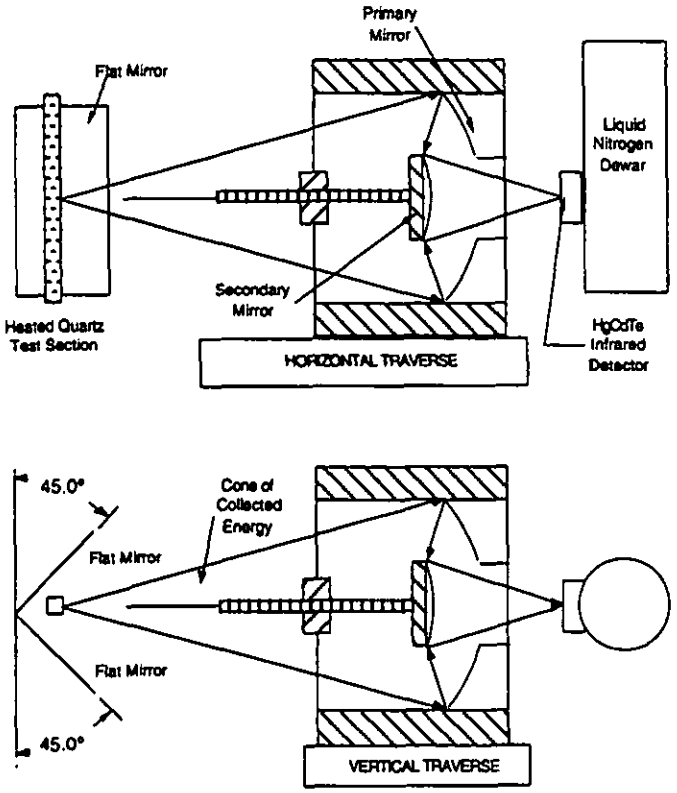

Figure 5: Schematic of Infrared Imaging System for Wall Temperature Measurement

To acquire a signal, the sensor and optics are moved to a desired location and remain fixed while the heated test section is rotated in front of them. When the test section passes into the focal point of the optics, the radiation emitted from the heated surface is focused onto the sensor. The sensor produces a voltage signal proportional to the level of incident radiation. Using the Stefan-Boltzmann Law, $q_{rad} \propto T^4$, the temperature of this spot on the surface can be deduced. The AC coupled sensor has a response time on the order of microseconds which means that an entire row of data can be collected during a single pass of the test section. This data then represents the temperatures in a 1mm wide strip on one side of the test section, at a given x location.

Thermocouples are used to measure coolant inlet and exit temperatures. Using the measured exterior wall temperature and ITO film heat flux, the interior wall temperature and heat flux are computed with a 3-D conduction algorithm. This algorithm accounts for variations in the thermal conductivity of quartz with temperature and is reported in Bons (1997). Nu is then calculated with an absolute uncertainty of 9%.

The Nd:YAG laser used emits two sequential 200mJ pulses with a nominal pulse width of 10ns (λ= 532nm). Pulse separations of 25-35μs were used in this research. Figure 6 is a schematic of the optical path. The spherical focusing lens and the final mirror are mounted on an optical traverse so the sheet can be moved from side to side in the test section passage (0<y/d<1). Approximately 16cm beyond the final mirror and just before the laser entry port is a cylindrical lens which expands the beam in only one direction to produce a planar sheet normal to the axis of rotation. The sheet thickness at the test section was measured to be 0.4 ±0.1mm with a height of 4cm. Gonesh #2 incense was used to seed the flow (particle diameters ≈ 0.4μm [Bryanston-Cross and Epstein, 1990]) and images were captured using a CCD camera located at the camera view window indicated in Figure 6. The image acquisition system is synchronized so that the laser fires and the camera forms an image only when the rotating test section is located in the camera's field of view.

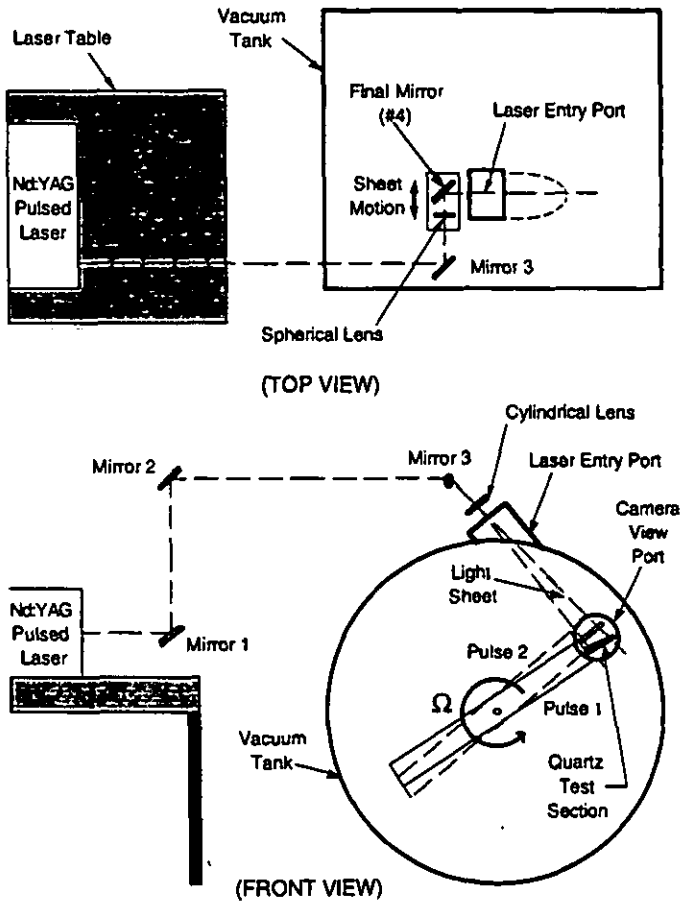

Figure 6: Schematic of Laser and Optical Layout

Particle Image Velocimetry (PIV) relies on sequential bursts of light to provide two frozen images of particles in a flowfield. Particles are paired with their double (or correlations are performed) to yield the net motion in the two dimensions of the light sheet. An accurate knowledge of the pulse time separation then provides two components of velocity. Because the camera is stationary relative to the test section, the second test section image is

displaced by an angle $\Omega\Delta t$ about the axis of rotation. To remove this angular displacement from the image, an alignment cross made from 13μm wire is inserted into the test section prior to testing. The camera then acquires a double-image of the rotating alignment cross. The pixel distance between the two cross images, the cross' radial position from the axis of rotation, and the $\Omega\Delta t$ for the cross image are sufficient to compute the center of rotation coordinates in "pixel space". Subsequent PIV images can then be "derotated" an angle $\Omega\Delta t$ about this pixel center of rotation provided the camera is not moved from its alignment position. The principle is similar to the bias-velocity added to images in some PIV applications to remove directional ambiguity (Jefferies, 1996). With this angular displacement removed from the image, the flow velocity relative to the rotating test section is determined. The uncertainty in the velocity vectors presented here was calculated to be 6%. The derotation contributes an additional 5% of bias error to all PIV images processed with the same pixel center measurement. A more detailed description of the experimental facility and data acquisition process can be found in Bons (1997).

ANALYTICAL MODEL

A momentum integral model of the rotating, heated passage flow was developed to aid in the interpretation of the velocity data. The model assumes that the passage flow can be dissected into independent shear flows on each of the four passage walls and a central inviscid "core" region. The entry length for turbulent pipe flow is 10 to 15 diameters, so the flow in this turbine cooling passage (with l/d < 15 and a short tapered inlet orifice) is modeled as developing turbulent flow. This methodology has been used with success by Mori and Nakayama (1968), Ito and Nanbu (1971), and more recently by Chew (1993) in analyzing rotating internal flows.

With this premise of developing turbulent flow, the boundary layers on each of the four contiguous passage walls grow independently with distance from the inlet. When the passage is not rotating, the only mutual influence they have is to jointly close-off the "core" flow region, thus accelerating the fluid in the center of the passage. The boundary layer growth is calculated using the momentum integral equation (Kays and Crawford, 1980):

$$\frac{\tau_o}{\rho_o u_\infty^2} + \frac{\rho_o v_o}{\rho_\infty u_\infty} = \frac{d\theta}{dx} + \theta\left[\left(2+\frac{\delta_d}{\theta}\right)\frac{1}{u_\infty}\frac{du_\infty}{dx}\right]$$

For turbulent flow, a power law shear stress relation is assumed.

$$u^+ = 8.75\left(y^+\right)^{1/n}$$

Substituting this into the momentum integral equation and integrating from x=0 to a point x>0 in the flow passage, with the initial condition that θ(x=0) = 0, produces an expression for θ(x).

$$\theta(x) = f(u_\infty, n, v)\left\{\int_0^x u_\infty^{g(n)}dx\right\}^{n+1/n+3}$$

The functions f and g are lengthy algebraic expressions resulting from the integration and can be found in Bons (1997). Assuming constant inlet velocity and temperature profiles, the boundary layer thickness can be calculated at any point downstream. The effect of the boundary layer growth on the core flow is assessed by applying conservation of mass to the passage cross-section. The core flow velocity rises as the blockage due to the wall layers increases down the passage.

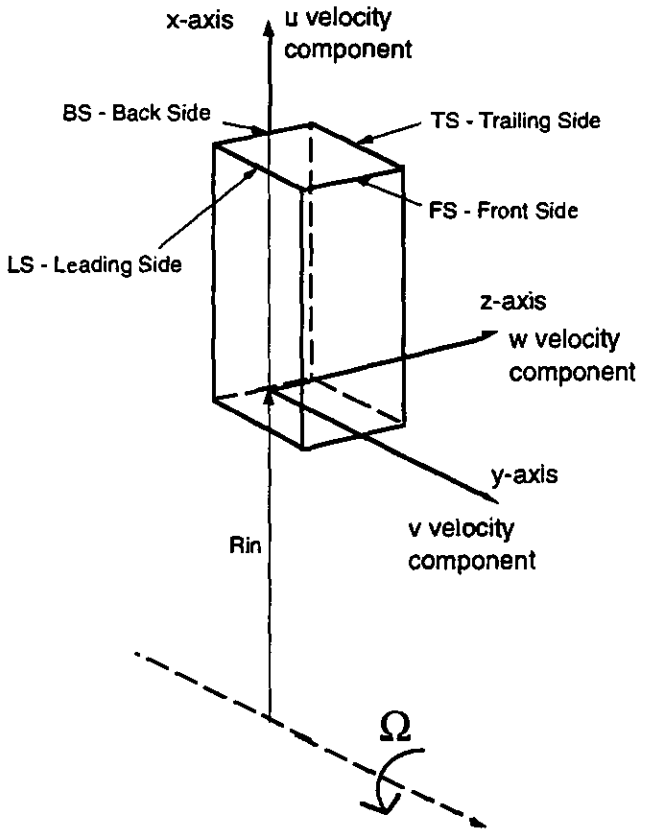

Figure 7: Schematic of Test Section Axis and Velocity Components

With this as the basic flow model, the multiple effects of rotation are assessed using the full Navier-Stokes equations for steady, incompressible flow evaluated in a coordinate system fixed to the passage as shown in Figure 7.

$$\left(\vec{u}\cdot\vec{\nabla}\right)\vec{u} + \frac{\partial\left(\overline{u_i u_j}\right)}{\partial x_j} = \nu\nabla^2\vec{u} - \frac{\nabla p}{\rho} - 2\vec{\Omega}\times\vec{u} + \beta\left(T-T_\infty\right)\left(\vec{\Omega}\times\vec{\Omega}\times\vec{R}\right)$$

where $\vec{u} = u\hat{i} + v\hat{j} + w\hat{k}$, $\vec{R} = (R_{in}+x)\hat{i} + y\hat{j} + z\hat{k}$, and $\vec{\Omega} = \Omega\hat{j}$.

Here the Boussinesq (1930) approximation has been applied, so the density variation is shown only in the buoyancy source term.

The $-2\vec{\Omega}\times\vec{u}$ term is the coriolis acceleration which accounts for the use of a non-inertial reference frame attached to the rotating passage. This coriolis acceleration term has a $+2\Omega u$ contribution to the z-momentum equation which generates a pressure gradient in the crossflow direction (Moore, 1967)

$$\frac{dp}{dz} = 2\Omega u_\infty \rho_\infty$$

Substituting this pressure gradient into the z-momentum equation, and solving for dw/dx (ignoring all other terms but the $+2\Omega u$ coriolis term) yields an expression for Δw_{cor} (the added coriolis-induced flow component for a Δx step down the passage).

$$\Delta w_{cor} \equiv 2\Omega\left[\frac{u\rho}{u_\infty \rho_\infty} - 1\right]\Delta x$$

In the side wall boundary layers, the conditions $up < u_-\rho_-$ and $\Delta w_{cor} < 0$ create the well-documented coriolis double vortex associated with pipe flow rotating in the orthogonal mode. The model generates the complete vortex by forcing w_{cor} to satisfy the crossflow conservation of mass ($\int w dy \equiv 0$) and the no-slip condition at the sidewalls (w(y=0&d)=0).

One result of this vortex is the convective transport of high momentum core fluid into the trailing wall boundary layer. This transport energizes the boundary layer here, thus reducing its thickness. Likewise, momentum deficit (low momentum trailing wall boundary layer fluid) is convected from the trailing wall to the side wall, and from there to the leading wall. The leading wall boundary layer then becomes the repository for the momentum deficit convected from the other walls. To account for these effects, the magnitude of convected momentum deficit is assessed at each step, and the boundary layer thickness of each passage wall is then adjusted up or down depending on the sign of the convection (up for the leading wall and down for the trailing wall).

The coriolis acceleration also contributes a $-2\Omega w$ term in the x-momentum equation which is incorporated into the model by assessing the associated increment of streamwise acceleration Δu_{cor}.

$$\Delta u_{cor} \equiv -2\Omega \frac{w\rho}{u_\infty \rho_\infty}\Delta x$$

From this relation, it is evident that in the region near the side wall (where w<0), this component results in an acceleration, whereas in the core region (where w>0) there is a corresponding deceleration. This effect is not linear with rotational frequency, since $w \propto \Omega$ it follows that $\Delta u_{cor} \propto \Omega^2$.

The buoyancy acceleration term contributes a $-\Omega^2 z\beta(T-T_-)$ term in the z-momentum equation which produces a positive acceleration on fluid near the leading wall ($T>T_-$ in the boundary layer and z<0 for the leading wall). Likewise for the trailing wall (where z>0), this acceleration (now of negative sign) accelerates hot trailing wall fluid toward the passage center. This buoyancy-induced center-seeking flow is modeled as mass injection from the wall into the boundary layer with normal velocity, v_e. Substituting this into the momentum integral equation, the net effect is to thicken both the trailing and leading wall boundary layers for d.r. > 0. This in turn creates a greater core acceleration.

The buoyancy acceleration term also contributes a $-\Omega^2 (R_{in}+x)\beta(T-T_-)$ term in the x-momentum equation which actually opposes the mean flow direction. Hot boundary layer fluid near the walls is accelerated in toward the axis of rotation while colder core fluid is accelerated away from the axis of rotation. The model incorporates this buoyant flow by allowing a region of separated flow to form near the leading wall. The separated region's spatial extent matches the mass defect of the buoyant flow and essentially pushes the turbulent boundary layer away from the physical wall to a point inside the passage. The other three walls are subjected to strong secondary flows and are considerably thinner, so the buoyancy associated with each of them is either convected to the leading wall or mixed into the respective boundary layer thickness. Experimentally measured wall temperature data and surface heat flux values are used to initiate the model. Comparisons with the measured flowfield are shown in the next section.

RESULTS AND DISCUSSION

The experimental data is presented in two parts: first the PIV fluid velocity measurements and second the passage wall Nusselt measurements. For the PIV images, the orientation of the light sheet allows access to a plane normal to the axis of rotation (x-z plane, see Figure 7). Since the strongest velocity gradients are expected in the y and z (non-radial) directions the vector field from each PIV image is first averaged along the x direction (yielding u(z) and w(z) for each image). Due to observed randomness in the vectors, four to six images at each location are combined to produce ensemble-averaged u(z) and w(z) distributions at a given x and y position. The light sheet and camera are then translated in the y and x direction to obtain ensemble averaged u(z) and w(z) distributions at various positions in the flow. u(z) and w(z) at the same x but various y positions can be "stacked-up" to provide a quasi-3D look at the flowfield (assuming the mean flow is steady). Then u(y) and w(y) distributions can be generated at this same x location by interpolating between images in the y direction.

Stationary Velocity Measurements. Figure 8 shows u(y) and w(y) data for Re=10000 and Rot=0 at two x/d locations. The model results are also indicated on the figure. Both the features of boundary layer development and core acceleration are evident in the u(y) data. The w(y) data show no significant transverse component when the passage is not rotating, and the model (not shown) predicts none.

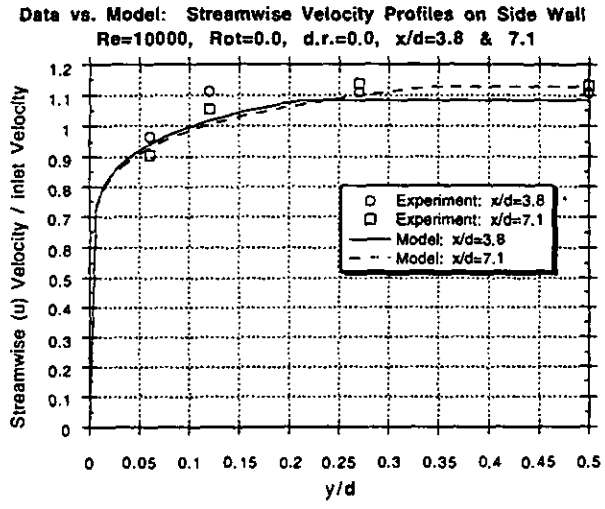

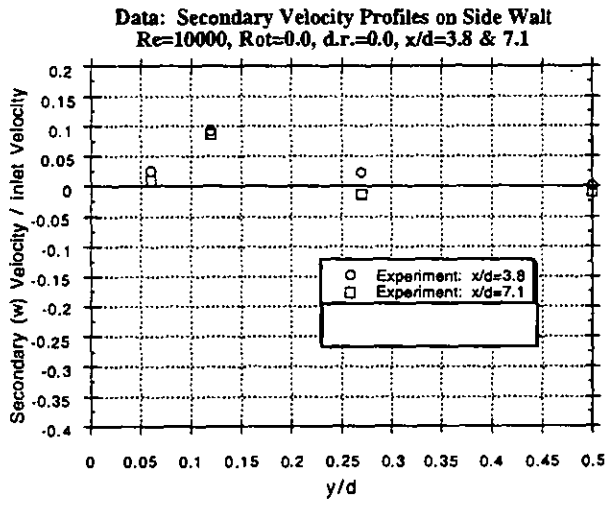

Figure 8: Streamwise u(y) and Secondary w(y) Velocity Profiles with Rot=0.0 & d.r.=0.0

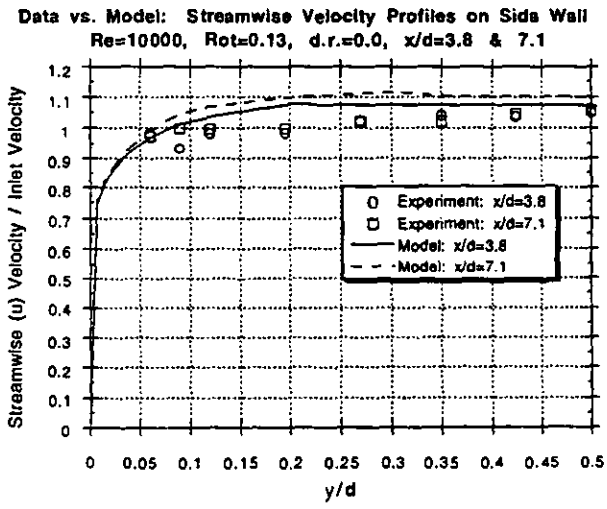

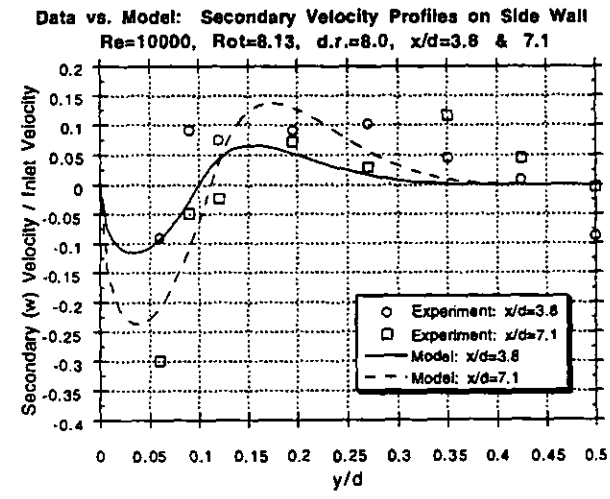

Figure 9: Streamwise u(y) and Secondary w(y) Velocity Profiles with Rot=0.13 & d.r.=0.0

Rotating Velocity Measurements. Data taken at the same Reynolds number and x/d positions, but with Rot=0.13, are shown in Figure 9. From the w(y) data, it is clear that a secondary vortex flow is present. The strength and spatial extent of this vortex grow noticeably with x/d. The peak negative w velocity has increased by a maximum factor of 3 with a doubling of distance from the passage inlet (x/d=3.8 vs. 7.1). Also, the crossover point to positive w occurs near y/d=0.13 at the downstream position vs. 0.07 for the upstream position. This is the effect of the Coriolis acceleration component in the z-momentum equation. The model calculations also show this vortex growth. The most notable feature in the u(y) data is the thinner boundary layer compared to the non-rotating case. The axial velocity is essentially flat from y/d=0.05 to mid-passage with only a modest rise beyond y/d=0.2. In addition, the core acceleration with x/d that was evident in the stationary case is negligible here. The mechanism responsible for this result is the streamwise (x-momentum) component of the Coriolis acceleration. This acceleration produces additional streamwise momentum in the near wall region where w<0 and depresses the velocity in the core region.

More striking evidence of this effect is seen in a similar data set for Rot=0.2 (Figure 10). Here the model calculations are plotted with and without the streamwise Coriolis effect (both incorporate the z-momentum component). The u(y) data now show a dramatic rise approaching the wall rather than the flat profile witnessed for Rot=0.13. Since u_{cor} is proportional to Ω^2 rather than simply Ω, a 60% rise in rotational frequency (from Rot=0.13 to 0.2) actually produces a rise in u_{cor} by a factor of 2.4. This also creates a depression of the core velocity relative to no rotation. The w(y) data in figure 10 show that the vortex has also been squeezed closer to the wall, and the corresponding crossflow velocities have nearly doubled. As further evidence of the streamwise coriolis effect, the model calculation with Coriolis incorporated is more in line with the experimental results.

Figure 11 shows the u(z) calculation vs. the experimental data for the same case with larger Rot= 0.2. The boundary layer

disparity between the trailing and leading walls is apparent. The vortex motion has thinned the trailing wall boundary layer and thickened the leading wall boundary layer. By incorporating this convection of boundary layer fluid into the model, the calculation matches the experimental data almost exactly. Other researchers have noted these same flow features to varying degrees. Berg et al. (1991) measured the velocity field in a long l/d rotating pipe (Re=40000 and Rot=0.04) with laser 2-focus and found a rise of 10% in the streamwise velocity from passage centerline to sidewall and a trailing-to-leading wall edge velocity ratio of 1.15. Tse and McGrath's (1995) LDV data show secondary velocity magnitudes up to 65% of the streamwise velocity at x/d=7 for Re=25000 and Rot=0.24. The streamwise velocity rise toward the side walls is also evident in their data.

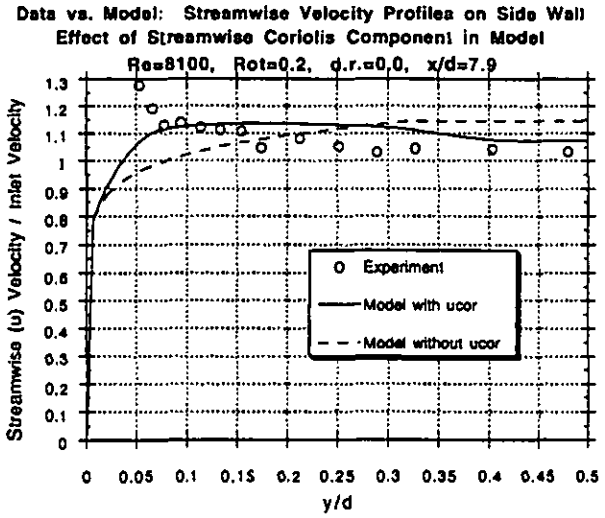

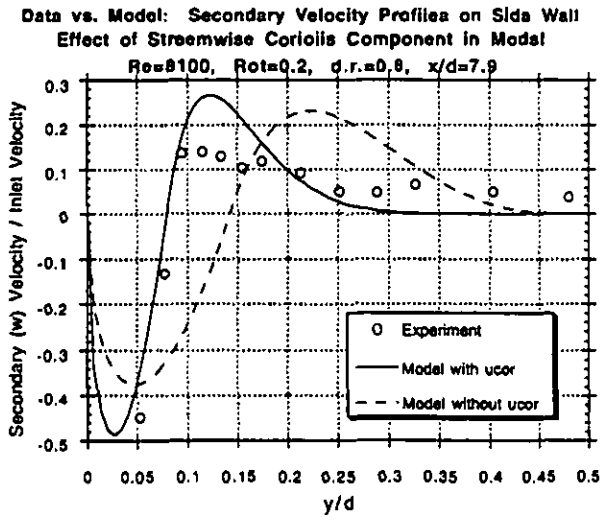

Figure 10: Streamwise u(y) and Secondary w(y) Velocity Profiles with Rot=0.2 & d.r.=0.0. Effect of Streamwise Component of Coriolis Acceleration in Model.

Finally, typical velocity vector fields from the centerline (y/d = 0.58) and near-wall (y/d = 0.93) rotating data are shown in Figure 12 for the Rot=0.2 case. The near wall vectors show the strong motion in the direction of rotation vs. the centerline vectors which are leaning in the opposite direction. The y/d=0.93 vectors also show evidence of the steep dw/dy gradient captured by the finite laser sheet thickness (0.4mm). Vectors with w/u_{in} = -0.5 lie side by side with w/u_{in} = 0.0 vectors in this 2D representation of a 3D flowfield.

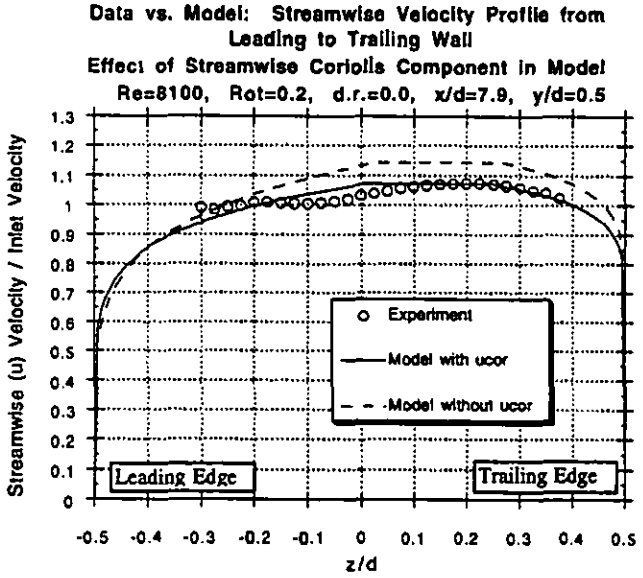

Figure 11: Data vs. Model Prediction of Streamwise u(z) Velocity Profiles with Rot=0.2 & d.r.=0.0. Effect of Streamwise Component of Coriolis Acceleration in Model.

<u>Heated, Rotating Velocity Measurements.</u> Figure 13 shows the effect of heat addition to the rotating flowfield. Plotted are u(z) distributions from 3 cases: Rot=0.0 & d.r.=0.0, Rot=0.2 & d.r.=0.0, and Rot=0.2 & d.r.=0.27 along with the model calculations. With heat addition, the trailing-to-leading wall disparity in streamwise velocity exceeds a maximum ratio of 2. This dwarfs the same measure from the non-heated data, shown in Figure 11 (and again in this figure) to be only 1.1 . Since Rot is identical in the two data sets, the distorted streamwise velocity profile for the heated case is clearly the result of hot, buoyant fluid collecting on the leading wall. The fact that the model calculation for the d.r.>0 case employs a separated leading wall profile and appears to match the trend in the data strongly suggests stagnant or reverse flow near the leading wall for these conditions. Unfortunately, it is difficult to optically image the near-wall region on the leading face of the test section due to surface reflections, but isolated vectors from a few selected PIV images do indicate the presence of stagnant or reversed flow. Figure 14 shows actual vector fields for the d.r.=0.27 case where the u(z) gradient and sites of stagnant flow along the leading wall are evident. The Coriolis vortex evident in the w(y) data of Figure 13 is responsible for the disproportionate effect of buoyancy on the leading wall. The hot

wall fluid from the trailing and side walls all collects on the leading wall due to the convective action of the swirling vortex.

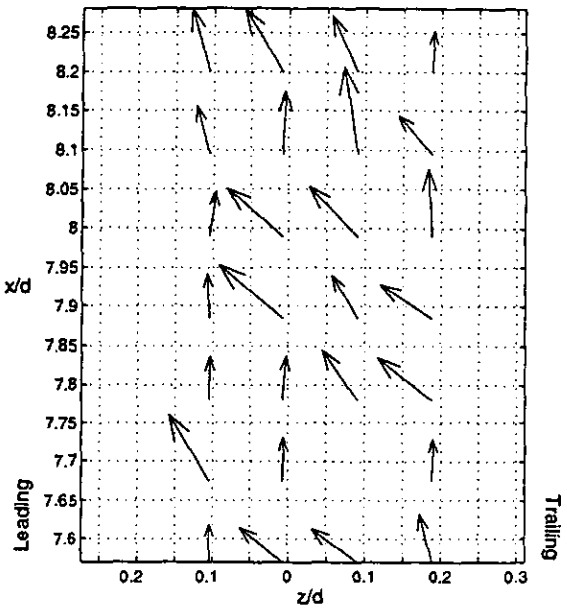

Velocity Vectors at y/d=0.93, mean u/u_{in} = 1.21, mean w/u_{in} = -0.57

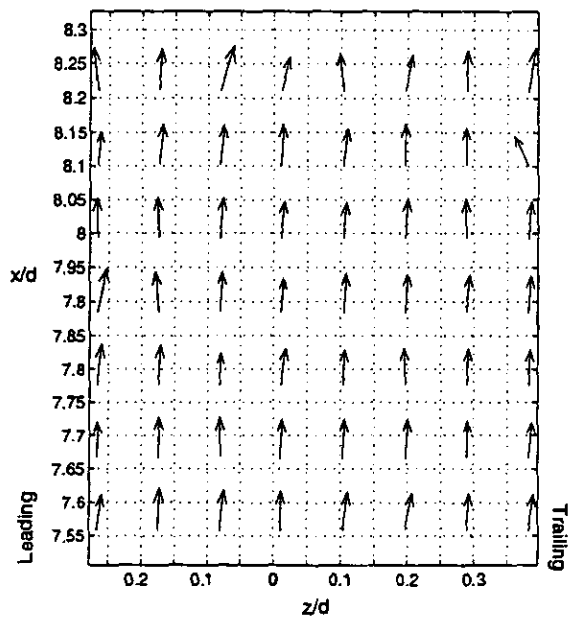

Velocity Vectors at y/d=0.58, mean u/u_{in} = 1.04, mean w/u_{in} = +0.06

Figure 12: Sample PIV Vector x-z Plots for Re=8100, Rot=0.2, & d.r.=0.0 at x/d=7.9.

Since there is no other heated rotating velocity data to compare this new data with, the results of several computational studies which give evidence of similar flow features are discussed for comparison. Dutta et al. (1994) computed a heated, rotating flowfield for Wagner and Johnson's configuration at Re=25000,

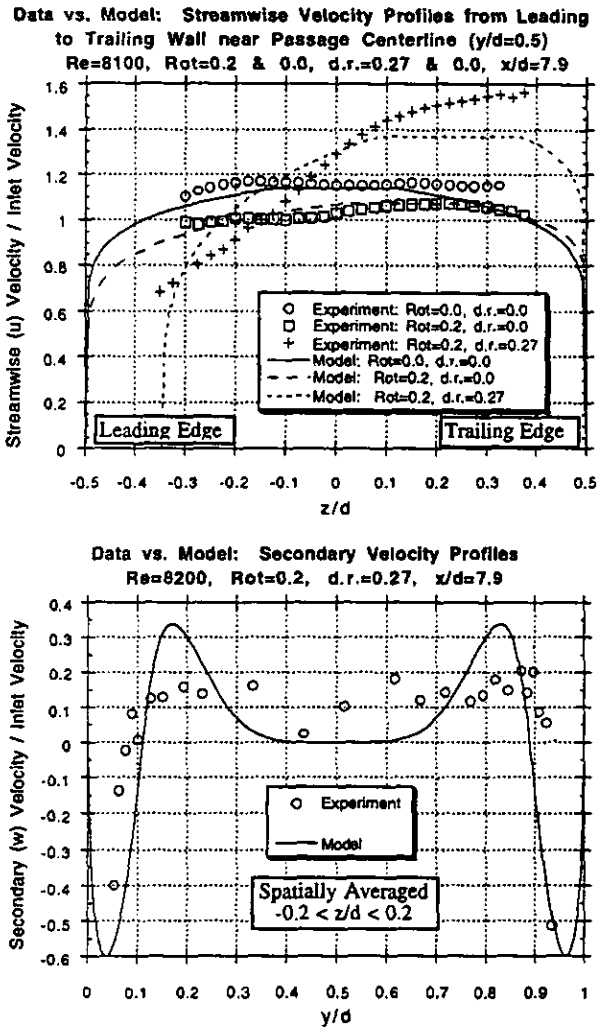

Figure 13: Streamwise u(y) and Secondary w(y) Velocity Profiles with Rot=0.2 & d.r.=0.27.

Rot=0.24, and d.r.=0.13 at x/d=9. The code results predict a streamwise velocity of $0.7u_{in}$ at z/d=-.35 and $1.2u_{in}$ at z/d=+0.35. Also, vectors near the side walls have secondary velocity magnitudes near $0.15u_{in}$ and an estimated vortex eye position of y/d=0.1. For the same conditions, but a lower Rot=0.12, Tekriwal (1996,1997) predicted nearly a factor of 2 in streamwise velocity from trailing side to leading side and shows cross-stream velocities near 0.2 u_{in} with a vortex eye position of y/d=0.15. At a higher Rot=0.48, Tekriwal predicted reverse flow over a region extending to $\Delta z/d$=0.15 from the leading wall. Prakash and Zerkle (1992) also predicted reverse flow for this same high Rot case. Finally, Bonhoff et al. (1997) predicted reverse flow and a peak streamwise velocity of $1.8u_{in}$ near the trailing wall for Rot=0.24, Re=25000, and d.r.=0.15. Though the three codes all predicted similar results (reverse flow and core velocity skewed to trailing wall), the published data are for three very different passage locations: x/d=8 for Tekriwal, x/d=2 for Prakash and Zerkle, and x/d=14 for Bonhoff et al.. The data presented here are at an x/d=8, a lower Re=10000, a

moderate Rot=0.2, and a factor of two higher d.r.=0.27 from the above predictions. While a CFD prediction reproducing these exact flow conditions is not yet available, this comparison shows that the measured behavior is in the range of that previously predicted.

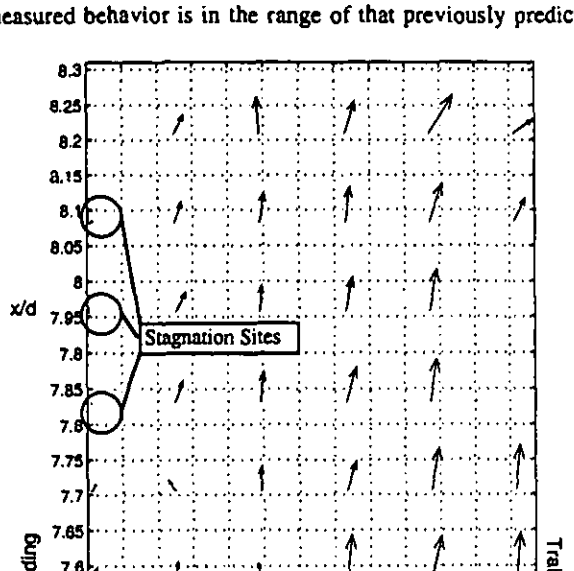

Velocity Vectors at y/d=0.85, mean u/u_{in} = 1.06, mean w/u_{in} = +0.24

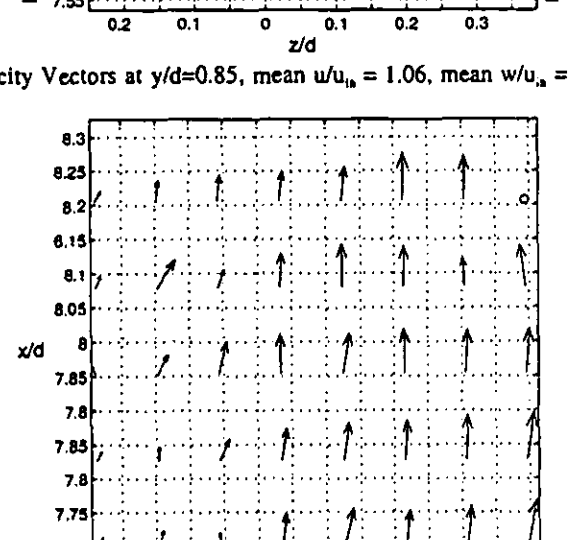

Velocity Vectors at y/d=0.79, mean u/u_{in} = 1.20, mean w/u_{in} = +0.12

Figure 14: Sample PIV Vector x-z Plots for Re=8200, Rot=0.2, & d.r.=0.27 at x/d=7.9.

The Coriolis effect on the streamwise velocity is also present in the heated PIV data, though now it competes directly with the buoyancy force on the side walls. Figure 15 shows u(z) profiles at various y stations. The region of highest velocity is 0.1<z/d<0.3 and y/d=0.1 (near the back side wall). The region of lowest velocity is -.3<z/d<-0.1 and y/d=0.86 (near the front side wall). This unexpected side-to-side asymmetry is due to the heating imbalance mentioned earlier in the experimental facility section. Due to a manufacturing error, the front side wall has a higher heat flux than the back side wall. Because of this, buoyancy has a stronger effect on the front side wall than the back side wall, and streamwise velocities along this wall (y/d=1) are lower. Upon closer inspection of the near-wall secondary velocities (w) in Fig 13, the peak negative velocity on the front side wall (y/d=1) is 20% higher than on the back side wall (y/d=0). Also, the region of positive w velocity extends further from the front wall than from the back side wall. Since the boundary layer to core fluid density ratio also influences w_{cor}, the stronger vortex on the front side wall is evidence of the heat load disparity between the two side walls. This combination of stronger vortex and greater buoyancy sharply reduce the heat transfer at the front side edge of the leading wall as will be seen shortly.

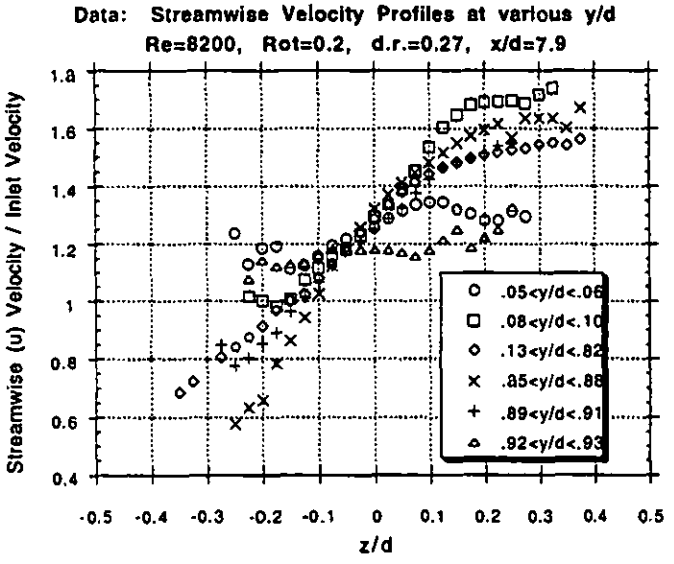

Figure 15: Streamwise u(z) Velocity Profile Data for Re=8200, Rot=0.2, & d.r.=0.27 at 6 y/d locations and x/d=7.9.

Before presenting the heat transfer data, it is instructive to attempt a heat transfer prediction based on the velocity data alone. Comparing the leading and trailing walls, and ignoring for the moment that the data suggests separation on the leading face due to buoyancy, we could estimate the Nusselt number for each side based solely on their associated boundary layer edge velocity. From Figure 13 this ratio appears to be approximately 2.2 (trailing wall-to-leading wall respectively). Following the analytical Dittus-Boelter (1930) correlation between Re and Nu, we would expect

$$\frac{Nu_{TS}}{Nu_{LS}} \propto \left\{\frac{Re_{TS}}{Re_{LS}}\right\}^{0.8} = \left\{\frac{u_{\infty TS}}{u_{\infty LS}}\right\}^{0.8} \equiv 2.2^{0.8} = 1.88$$

As will be shown subsequently, this is within 6% of the experimentally measured Nu ratio at this x/d.

Heat Transfer Measurements. The plots of Nu shown here are normalized by the Dittus-Boelter correlation for Nu in a stationary tube.

$$Nu_{\infty} = 0.023\,Pr^{0.4}\,Re^{0.8}$$

Data is presented for 0.02<Rot<0.29 all at Re≅8200 and d.r. ≅0.27.

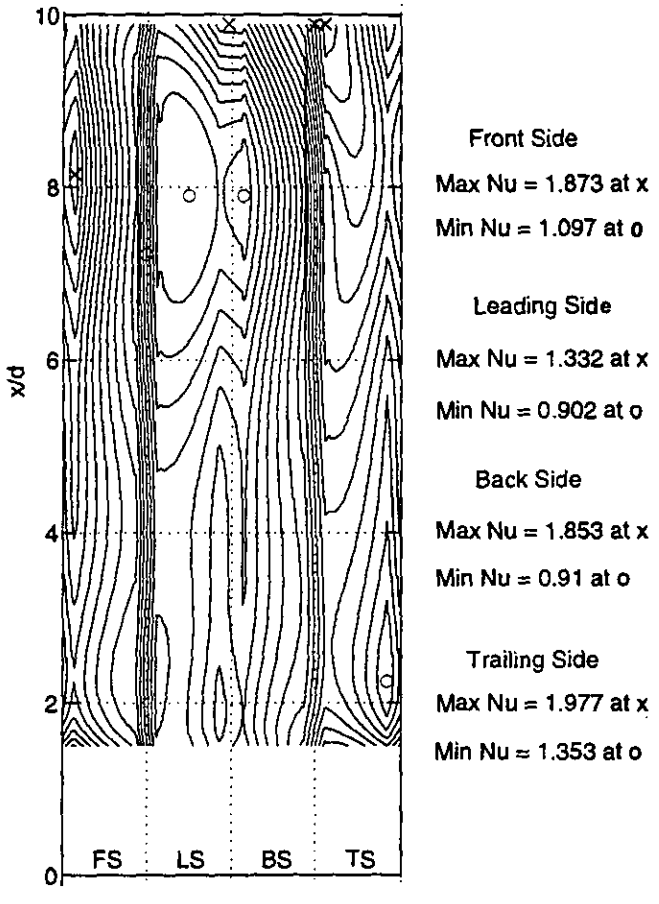

Figure 16: 0.05 Nu/Nu$_\infty$ Contours on Inside of Passage for Re=8222, Rot=0.191, & d.r.=0.27.

Figure 16 shows the Nusselt ratio contours on the inside walls of the test section for the same conditions used in the heated PIV study just presented. The four walls are displayed in succession from left to right: front side wall (y/d=1), leading wall (z/d=-0.5), back side wall (y/d=0), and trailing wall (z/d=+0.5) (see Figure 7). A low Nu spot is evident on the leading wall at x/d=8 and a corresponding high Nu region is located on the trailing wall at the same x/d. The Nu on the other sides appears to vary monotonically between the leading and trailing wall peak values. Upon closer inspection, the low Nu region on the leading wall is skewed to the front side wall rather than the back side wall and the lateral Nu gradient on the front side wall appears steeper than that on the back side wall. This is evidence of the disparity in surface heat flux between the two walls. The increased heat addition on the front wall produces more buoyant hot fluid which collects on the leading wall creating the skewed Nu map. Also, the vortex is stronger along this wall causing a steeper Nu gradient than on the back wall. If a symmetric heat flux wall condition had been achieved, the authors would expect the flow and Nu measurements to exhibit greater symmetry about the passage centerline (y/d=0.5).

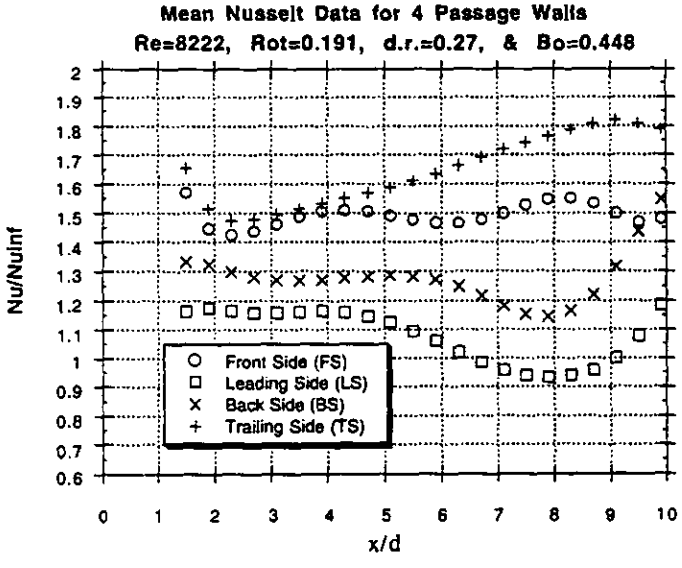

Figure 17: Mean Side Nu(x)/Nu$_\infty$ for all 4 Walls. Re=8222, Rot=0.191, & d.r.=0.27.

The magnitude of these two effects is more clearly evaluated with Figure 17 which shows the side mean Nu as a function of x. As expected $Nu_{TS} > Nu_{LS}$ by nearly a factor of 2 at x/d=8. This nearly matches the edge velocity prediction made earlier. While Nu_{TS} climbs nearly linearly from inlet to exit, Nu_{LS} is flat until x/d=5 and then drops to a low at x/d=8. As the velocity data indicated, the buoyancy effect is considerable at x/d=8, creating a huge disparity between the flowfield on the leading wall vs. the trailing wall. If a region of separated flow on the leading wall is the flow feature causing this low Nu at x/d=8, it is logical to pick a separation point based on the Nu data alone at approximately x/d=5 (since this is where Nu_{LS} begins to drop). Extrapolating further, there may be a flow reattachment at x/d=9, as Nu_{LS} begins to rise here. x/d=9 is also near the passage exit (l/d=11.5), so this rise may be due to a recirculating flow from the exit plenum.

The comparison of the front and back wall Nu ratios is more complex. On the average, Nu_{FS} is 15% greater than Nu_{BS}. The greater heat load added on the front side appears to have the primary effect of strengthening the vortex here, thus creating an increased convective heat transfer and higher Nu. There are also noticeable oscillations in the Nu data. Nu_{FS} initially rises with Nu_{TS} but drops down coincident with the drop off in Nu_{LS} at x/d=5. Then, there is a

reprieve from x/d=6 to 8 where Nu_{FS} rises and Nu_{BS} drops. Finally, Nu_{FS} drops to the exit and Nu_{BS} overtakes Nu_{FS}.

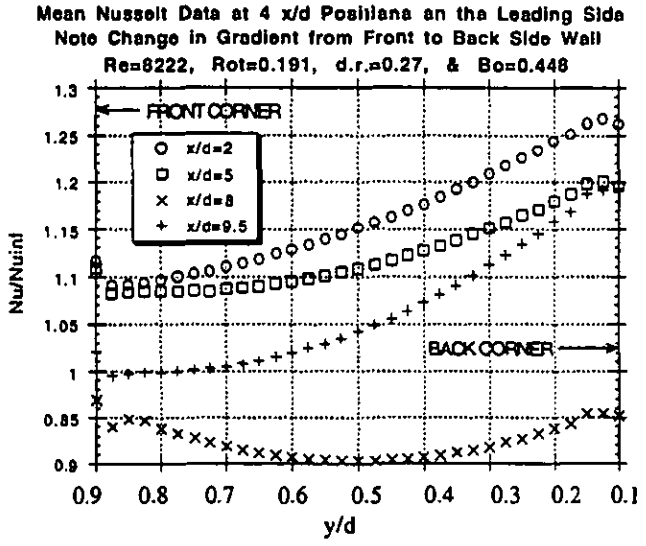

Figure 18: $Nu(y)/Nu_{\infty}$ along Leading Wall at 4 x/d Stations. Re=8222, Rot=0.191, & d.r.=0.27.

To get some idea as to what may cause these apparent oscillations, Fig 18 shows plots of Nu(y) at various x locations on the leading wall. Clearly the Nu_{LS} profile flattens around x/d=8, while before and after this point Nu_{LS} is lower near the front side edge. One possible explanation is the collection of a strong buoyancy-generated separation bubble near the front-side/leading wall corner due to the heating imbalance. As the bubble grows with x/d it slowly migrates laterally until it fills the whole passage width (creating the flat Nu_{LS} profile near x/d=8). At this point, no further migration is possible and buoyant fluid again collects disproportionately on the front side/leading wall edge. The result is a reduced Nu here after x/d=8. Han and Zhang (1992) found that when a wall-to-wall heating imbalance (uneven wall temperatures) was imposed on a rotating coolant passage, Nu was higher on all of the passage walls compared with the constant wall temperature case (at the same density ratio). They postulated that the buoyancy imbalance destabilizes the core flow, creating a lateral motion that could give rise to Nu variations like those seen here. Another explanation could be the presence of a characteristic "Helmholtz-like" fluid instability due to the buoyant rotating flow: the bulk flow moving side-to-side in the passage alternating between the front and back side walls. Either of these would account for the Nu oscillations in Fig 17, but more data is needed to confirm their validity.

Figures 19 and 20 show the effect of rotation number on the ratio Nu_{TS} / Nu_{LS} and the average value $Nu_{avg} = (Nu_{LS}+Nu_{TS})/2$. Though PIV data was taken only for Rot=0.2, trends in the Nu data with Rot can be interpreted by extrapolating from the available velocity data. If as speculated, separation caused the rise in Nu_{TS} / Nu_{LS} at x/d=5 for Rot =0.2, perhaps at the highest rotation, flow separation on the leading wall begins at x/d=2 (where Nu_{TS} / Nu_{LS} rises dramatically in Figure 19). Then beyond x/d=5, the separated region may have collapsed causing flow to move back toward the leading wall and decreasing Nu_{TS} / Nu_{LS}. From both figures it is clear that the passage mean Nu and the trailing-to-leading wall Nu disparity grow with Rot.

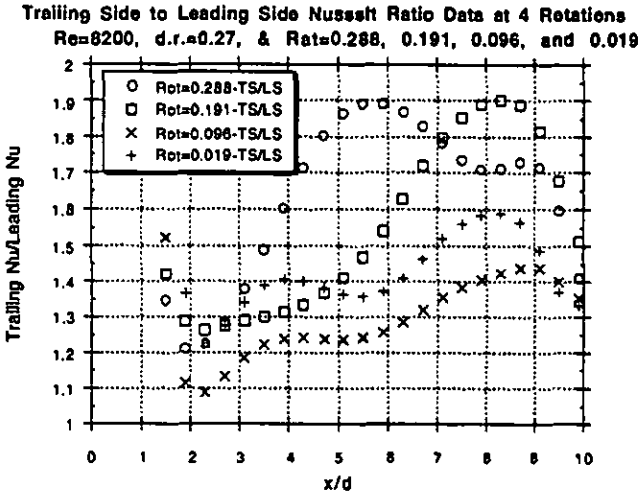

Figure 19: Mean Side Trailing-to-Leading Wall Nu Ratio for 4 Rot: 0.288, 0.191, 0.096, & 0.019.

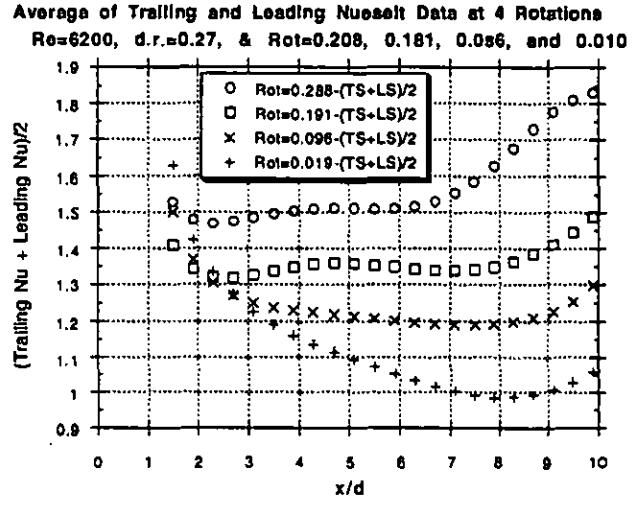

Figure 20: Mean Side Trailing + Leading Wall Nu Ratio Average for 4 Rot: 0.288, 0.191, 0.096, & 0.019.

Data taken by Barry (1994) on the same facility show a nearly identical trend for Nu_{TS} / Nu_{LS}, though the Barry data is at Re=25000. The ratio rises to approximately 2 by x/d=8 and drops off toward the exit. Guidez (1989) also measured a Nu_{TS} / Nu_{LS} ratio of 2 at x/d=7.4 and Re=24000, Rot=0.2, and d.r.=0.36. Wagner et al. (1991) show a Nu_{TS} / Nu_{LS} ratio of nearly 3.5 for Re=25000, Rot=0.2, and d.r.=0.22. Both the Guidez and Wagner et al. data show Nu_{TS} rising to a maximum at x/d=8 and Nu_{LS} dropping from inlet to x/d=6 (followed by a rise thereafter).

CONCLUSIONS

An experimental investigation was conducted on the internal flowfield of a simulated turbine blade cooling passage. Velocity measurements were taken using Particle Image Velocimetry for both heated and non-heated cases. Under the same conditions, an infrared detector collected wall temperature data for use in calculating local Nusselt number. The test section was operated with radial outward flow and at values of Reynolds number, Rotation number, and density ratio typical of applications. The conclusions of the study are as follows:

1) This work contains the first reported global velocity measurements in a heated, rotating test section. This successfully demonstrates the application of PIV to a rotating flowfield. In addition, high resolution heat transfer measurements taken with the same test section operating at the same conditions allow the direct correlation of flow phenomena with heat transfer phenomena.

2) The Coriolis vortex has two significant effects on the flowfield. It transports hot, low momentum wall fluid from the trailing wall to the side wall and finally to the leading wall of the square passage. Second, it creates a rise in streamwise velocity in the region near the side wall where the secondary flow is in the direction of rotation. The first of these two effects has the greatest impact on cooling. The accumulation of hot, low-momentum coolant near the leading wall effectively deters heat removal there.

3) The effect of buoyancy is also considerable, reducing streamwise velocities by a factor of 2 in regions where high temperature coolant is concentrated (near the leading wall).

4) A factor of 2 difference in Nu from trailing to leading wall arises due to the combination of these buoyancy and Coriolis effects. Without the Coriolis vortex, the buoyancy effect would be evenly distributed to all 4 walls. Without the buoyancy effect, the Coriolis vortex would only create a 10% shift in streamwise velocity toward the trailing wall (vs. 120% with buoyancy). Since the wall Nu appears to correlate directly with this edge velocity, a Nu prediction based solely on the Coriolis effect would have a factor of 2 error. This underscores the need for full simulation of both effects simultaneously.

5) A momentum integral model has proven to be a useful tool in flow interpretation. With several refinements incorporated from the experimental data, the model calculations are accurate to within 20% of the observed flow features. This lends validity to the underlying model assumption of an inviscid core flow surrounded by wall shear layers. Modeling the Coriolis vortex as a momentum deficit transport mechanism that primarily exchanges hot, low-momentum boundary layer fluid between adjacent walls was found to be a successful strategy. Modeling the buoyancy effect as a separated region of stagnant flow on the leading wall also matches the experimental observation well.

ACKNOWLEDGEMENTS

The authors wish to recognize the assistance of the technical staff at the Gas Turbine Laboratory, specifically Mr. James Letendre, Mr. Viktor Dubrowski, and Mr. William Ames, for the construction of the facility. Also, we acknowledge the professional advice and assistance offered by Dr. Gerald Guenette and Professor Edward Greitzer. This work was performed under partial sponsorship from the US Department of Energy and Solar Turbines Inc.

REFERENCES

Barry, P., 1994, "Rotational Effects on Turbine Blade Cooling", Master's Thesis, Department of Aeronautics and Astronautics, Massachusetts Institute of Technology, Cambridge, MA.

Berg, H., Hennecke, D., Elfert, M., and Hein, O., 1991, "The Effect of Rotation on Local Coolant Side Flow and Heat Transfer in Turbine Blades", ISABE 91-7016, published by AIAA, pp. 170-183.

Bonhoff, B., Tomm, U., Johnson, B., and Jennions, I., 1997, "Heat Transfer Predictions for Rotating U-Shaped Coolant Channels with Skewed Ribs and with Smooth Walls", ASME Paper #97-GT-162, presented at ASME IGTI, Orlando, Florida, June 2-5.

Bons, J., 1997, "Complementary Velocity and Heat Transfer Measurements in a Rotating Turbine Cooling Passage", PhD Thesis, Department of Aeronautics and Astronautics, Massachusetts Institute of Technology, Cambridge, MA.

Boussinesq, 1930, "Theorie Analytique de la Chaleur", Vol 2, Gathiers-Villars, Paris.

Boyer, D.L., 1965, "Flow through a Rapidly Rotating Rectangular Channel", PhD Thesis, The Johns Hopkins University.

Bryanston-Cross, P. and Epstein, A., 1990, "The Application of Sub-Micron Particle Visualisation for PIV at Transonic and Supersonic Speeds", Prog. Aerospace Sci., Vol. 27, pp. 237-265.

Chew, J., 1993, "A Momentum-Integral Solution of Flow in a Rotating Circular Duct", Int. J. of Heat and Fluid Flow, Vol. 14, No. 3, pp. 240-245.

Dittus, F.W., and Boelter, L.M.K., 1930, University of California Publications, Vol 2, pg. 443.

Dutta, S., Andrews, M., and Han, J.C., 1994, "Numerical Prediction of Turbulent Heat Transfer in a Rotating Square Duct with Variable Rotational Buoyancy Effects", presented at the 6th AIAA/ASME Thermophysics and Heat Transfer Conference, Colorado Springs, CO, June 20-23.

Guidez, J., 1989, "Study of the Convective Heat Transfer in a Rotating Coolant Channel", ASME Journal of Turbomachinery, Vol. 111, pp. 43-50.

Han, J. and Zhang, Y., 1992, "Effect of Uneven Wall Temperature on Local Heat Transfer in a Rotating Square Channel with Smooth Walls and Radial Outward Flow", ASME Journal of Heatr Transfer, Vol. 114, pp. 850-858.

Han, J., Zhang, Y., and Lee, C., 1994, "Influence of Surface Heating Condition on Local Heat Transfer in a Rotating Square Channel with Smooth Walls and Radial Outward Flow", ASME Journal of Turbomachinery, Vol. 116, pp. 149-158.

Hsieh, S., Chiang, M., Chen, P., 1997, "Velocity Measurements and Local Heat Transfer in a Rotating Ribbed Two-Pass Square Channel with Uneven Wall Heat Flux", ASME Paper #97-GT-160, presented at ASME IGTI, Orlando, Florida, June 2-5.

Iacovides, H. and Launder, B., 1991, "Parametric and Numerical Study of Fully Developed Flow and Heat Transfer in Rotating Rectangular Ducts", ASME Journal of Turbomachinery, Vol. 113, pp. 331-338.

Ito, H. and Nanbu, K., 1971, "Flow in Rotating Straight Pipes of Circular Cross Section", ASME Journal of Basic Engineering, pp. 383-394.

Jefferies, R.W., 1996, "Interactions of a Quasi-Two-Dimensional Vortex with a Stationary and Oscillating Leading-Edge", PhD Thesis, Department of Mechanical Engineering, Lehigh University, Pa.

Kays, W. and Crawford, M., 1980, *Convective Heat and Mass Transfer*, McGraw-Hill Book Company.

Mochizuki, S., Takamura, J., Yamawaki, S., and Yang, Wen-Jei, 1994, "Heat Transfer in Serpentine Flow Passages with Rotation", ASME Journal of Turbomachinery, Vol. 116, pp. 133-140.

Moore, J., 1967, "Effects of Coriolis on Turbulent Flow in Rotating Rectangular Channels", Gas Turbine Lab Report #89, Massachusetts Institute of Technology, Cambridge, MA.

Mori, Y. and Nakayama, W., 1968, "Convective Heat Transfer in Rotating Radial Circular Pipes (1st Report, Laminar Region)", International Journal of Heat and Mass Transfer, Vol. 11, pp. 1027-1040.

Morris, W. and Ayhan, T., 1979, "Observations on the Influence of Rotation on Heat Transfer in the Coolant Channels of Gas Turbine Rotor Blades", Proc. Insts. Mech Engrs. Vol 193, pp. 303-311.

Morris, W., 1981, *Heat Transfer and Fluid Flow in Rotating Coolant Channels*, Research Studies Press.

Morris, W. and Ghavami-Nasr, G., 1991, "Heat Transfer Measurements in Rectangular Channels with Orthogonal Mode Rotation", ASME Journal of Turbomachinery, Vol. 113, pp. 339-345

Prakash, C. and Zerkle, R., 1992, "Prediction of Turbulent Flow and Heat Transfer in a Radially Rotating Square Duct", ASME Journal of Turbomachinery, Vol. 114, pp. 835-846.

Tekriwal, P., 1996, "Effect of Aspect Ratio on the Buoyancy Driven Reverse Flow near the Leading Wall of Rotating Cooling Passages", ASME Paper #96-GT-173, presented at ASME IGTI, Birmingham, UK, June 10-13.

Tekriwal, P., 1997, "Heat Transfer Predicuons in Rotating Radial Smooth Channel: Comparative Study of k-e Models with Wall Function and Low-Re Model", ASME Paper #97-GT-162, presented at ASME IGTI, The Hague, Netherlands, June 13-16.

Tse, D. and McGrath, D., 1995, "A Combined Experimental/Computational Study of Flow in Turbine Blade Passage: Part 1 - Experimental Study", ASME Paper #95-GT-355, presented at ASME IGTI, Houston, Texas, June.

Tse, D. and Steuber, G., 1997, "Fow in a Rotating Square Serpentine Coolant Passage with Skewed Trips", ASME Paper #97-GT-529, presented at ASME IGTI, Orlando, Florida, June 2-5.

Uellner, S. and Roesner, K., 1991, "LSV Applied to the Flow in a Rotating Channel", ASME Laser Anemometry, Vol. 2, pp. 541-546.

Wagner, J., Johnson, B., and Hajek, T., 1991a, "Heat Transfer in Rotating Passages with Smooth Walls and Radial Outward Flow", ASME Journal of Turbomachinery, Vol. 113, pp. 42-51.

Wagner, J., Johnson, B., and Kopper, F., 1991b, "Heat Transfer in Rotating Serpentine Passages with Smooth Walls", ASME Journal of Turbomachinery, Vol. 113, pp. 321-330.

Wagner, J., Johnson, B., Graziani, R., and Yeh, F., 1992, "Heat Transfer in Rotating Serpentine Passages with Trips Normal to the Flow", ASME Journal of Turbomachinery, Vol. 114, pp. 847-856.

Wagner, R. and Velkoff, H., 1972, "Measurements of Secondary Flows in a Rotating Duct", ASME Journal of Engineering for Power, pp. 261-270.